JGR Space Physics

RESEARCH ARTICLE
10.1029/2024JA032478

Interaction of Cosmic Rays With Magnetic Flux Ropes

Alejandro Lara[1], **A. Borgazzi**[2], **Eduardo Guennam**[3], **Tatiana Niembro**[4], **and K. P. Arunbabu**[5]

[1]Instituto de Geofísica, Universidad Nacional Autónoma de México, Ciudad de México, México, [2]Departamento de Física, Facultad de Ciencias Exactas y Tecnología (FACET), Universidad Nacional de Tucumán, Tucumán, Argentina, [3]Departamento de Ciencias de la Computación, Facultad de Ciencias Exactas y Tecnología (FACET), Universidad Nacional de Tucumán, Tucumán, Argentina, [4]Smithsonian Astrophysical Observatory, Center for Astrophysics | Harvard & Smithsonian, Cambridge, MA, USA, [5]School of Environmental Studies, Cochin University of Science and Technology, Kochi, India

Abstract The heliosphere is full of galactic cosmic rays (GCR), high-energy charged particles coming isotropically from the galaxy. The GCR interact with the solar wind blown by the Sun carrying out plasma, magnetic fields and transient structures such as interplanetary coronal mass ejections (ICMEs) and their associated magnetic flux ropes (MFR). The GCR interaction with ICMEs has been extensively studied particularly the GCR flux attenuation (known as *Forbush decreases*) as a result of interacting with the ICME sheath and magnetic field. In this work, we investigate the opposite effect: the MFR's ability to generate GCR anisotropies which an observer may detect as an increase in the GCR flux. To achieve this, we simulated a flux of protons with energies in the 10–160 GeV range arriving from all directions to a cylindrical MFR (with and without sheath) with plasma, magnetic field, and spatial dimensions found in average ICMEs observed at 1 au. By following the individual trajectories of the injected particles we found that the MFR deviates the charged particles preferentially in one direction parallel to the MFR–axis. We also found that the peak of this anisotropic GCR flux depends on: the angle between the MFR and ambient magnetic fields; the presence or not of the sheath region; the energy of the incident particles and the observer location inside the MFR.

Key Points:

- We show that magnetic flux ropes associated to interplanetary coronal mass ejections produce anisotropies in the cosmic rays flux
- This finding helps to understand the anisotropies and enhancements of galactic cosmic rays (GCR) observed when magnetic clouds reaches the Earth
- Our numerical simulations can be extended to any scenery where cosmic rays interacts with magnetic flux ropes

Supporting Information:

Supporting Information may be found in the online version of this article.

Correspondence to:

A. Lara,
alara@igeofisica.unam.mx

Citation:

Lara, A., Borgazzi, A., Guennam, E., Niembro, T., & Arunbabu, K. P. (2024). Interaction of cosmic rays with magnetic flux ropes. *Journal of Geophysical Research: Space Physics*, *129*, e2024JA032478. https://doi.org/10.1029/2024JA032478

Received 23 JAN 2024
Accepted 28 JUL 2024

Author Contributions:

Conceptualization: Alejandro Lara, Tatiana Niembro
Formal analysis: Alejandro Lara
Investigation: A. Borgazzi
Software: Eduardo Guennam
Validation: K. P. Arunbabu
Writing – original draft: Alejandro Lara
Writing – review & editing: A. Borgazzi, Tatiana Niembro, K. P. Arunbabu

1. Introduction

Energetic processes within the galaxy drive the acceleration of charged particles to exceedingly high energy levels. These particles, known as galactic cosmic rays (GCR) reach the inner heliosphere as a quasi-stationary and -isotropic flux. The GCR flux is mainly composed of protons with energy ranging from a few tens of MeV to PeV, following a power-law spectrum E^{γ}, where $\gamma \sim -2.7$ (Gaisser et al., 2016) with small hardening at the "knee" ($\sim 3 \times 10^{15}$ eV) and a softening at the "ankle" ($\sim 3 \times 10^{18}$ eV).

The solar activity modulates the GCR flux in the lower part of the spectrum, from ∼30 MeV up to ∼150 − 300 GeV (depending on the solar cycle phase, Dorman, 2006), and throughout the entire heliosphere as shown by Voyager 1 and Voyager 2 missions (see Dialynas et al., 2023, and references therein). Along with the well-known long-term (11–22 years) solar modulation (e.g., Aslam & Badruddin, 2012, 2015; Thomas et al., 2014; Van Allen, 2000), short-term GCR modulations with time scales from hours to weeks are also observed in the GCR flux (e.g., Alania et al., 2011; Guo et al., 2021).

These short-term GCR modulations are mainly caused by the interaction of the GCR with the so-called Interplanetary Coronal Mass Ejections (ICME, Arunbabu et al., 2015; Dumbović et al., 2012; Bhaskar et al., 2016), which are large structures of plasma and magnetic field expelled by the Sun (e.g., Cane, 2000; Lara et al., 2005) and expand rapidly reaching widths at 1 au of few tents of au. When the ICME speed is higher relative to the ambient solar wind, the ICME usually have a three-part structure composed of a leading shock wave, followed by a turbulent sheath region and the driving structure (Luhmann et al., 2020) which often presents a core dominated by enhanced magnetic fields. When this driver exhibits a coherent helical configuration, we refer to them as magnetic flux-rope (hereinafter MFR, Burlaga et al., 1981; Nieves-Chinchilla et al., 2019), a very well studied ICME subset (Marubashi, 2000; Kilpua et al., 2019, and references therein).

The GCR–ICME interaction has been extensively studied regarding the decreases in the observed GCR flux known as Forbush decreases (FD, Arunbabu et al., 2013; Davies et al., 2023; Forbush, 1937). The FD magnitude depends on the particle energy and charge (i.e., rigidity, Cane, 2000) with decreases up to 25% with lower (few tents of GV) rigidity values. Commonly, FDs exhibit a step-like behavior over time that starts with a sudden

decrease that can last a few hours, followed by a gradual recovery of a few days (Cane, 2000) and a final restoration of the GCR flux to its pre-decrease value (Usoskin et al., 2008).

Several studies have been carried out to link the modulation of GCRs by ICMEs, and therefore the resulting FD profile, with the different substructures comprising an ICME. In some of them, the FD magnitudes have been estimated based on the GCR diffusion through the ICME turbulent sheath region (Arunbabu et al., 2013, 2015; Subramanian et al., 2008) while in others depending on the topology and the intensity of the ICME magnetic field (Petukhova et al., 2019). Moreover, the GCR–MFR interaction during FD events has been simulated numerically establishing that the decrease of particles inside the MFR depends on the magnetic field strength (Kubo & Shimazu, 2010) and the field outside the MFR (Laitinen & Dalla, 2021).

However, the GCR–MFR interaction has also been related to an opposite short-term solar modulations: GCR flux enhancements, which have been scarcely investigated. For instance, some studies have noticed that the GCR flux increases are observed before the arrival of ICMEs which have been identified as FD precursors and attributed to loss-cone mechanisms (Munakata et al., 2000; Rockenbach et al., 2011). It has also be found that some of these short-time (of a few hours) GCR flux increases seems to be connected to the passage of large interplanetary disturbances but were credited to changes in the geomagnetic field (Altukhov et al., 1963; Yoshida, 1959). A related phenomena are the anisotropies observed during some FDs (see Munakata et al., 2022, and references therein), which has been attributed to trapped particles inside MFRs, but there is no definitive explanation of this effect. And finally, recent high-accuracy measurements of the High Altitude Water Cherenkov (HAWC) array (Abeysekara et al., 2023; Alvarez et al., 2021) have established that the short-time GCR increases associated with the passage of an MFR at the Earth vicinity were due to GCR anisotropies caused by the alignment of the charged particles along the axis of the MFR (Akiyama et al., 2020).

To determine the origin of the short-time increases and/or anisotropies observed in the GCR flux associated with ICMEs, in this work, we follow the trajectories of protons with energy in the 10–160 GeV range when they enter into a helical magnetic field with strength and size similar to a typical MFR observed at 1 au.

2. Simulating the GCR–MFR Interaction

As it is known, the movement of charged particles in electromagnetic fields accounting for relativistic effects can be described by:

$$\frac{d\mathbf{u}}{dt} = \frac{q}{m}(\mathbf{E} + \mathbf{v} \times \mathbf{B}) \tag{1}$$

and

$$\frac{d\mathbf{x}}{dt} = \mathbf{v} \tag{2}$$

where $\mathbf{x}$ is the particle position, $\mathbf{u} = \gamma\mathbf{v}$ is the relativistic momentum vector divided by the particle rest mass m, $\gamma = 1/\sqrt{1 - v^2/c^2}$ is the Lorentz or relativistic factor, $\mathbf{E}$ and $\mathbf{B}$ are the electric and magnetic fields, respectively, and q is the particle electric charge (see Ripperda et al., 2018, for details).

The numerical time integration scheme employed in this work corresponds to the well-known Boris method (Boris, 1970), particularized for the case of the null electric field. The integration process consists in advance in time both, the position and velocity of the particle. Firstly, a particle half-position update is performed, after step n, for integration time step Δt:

$$\mathbf{x}^{n+1/2} = \mathbf{x}^n + \frac{\mathbf{u}^n}{2\gamma^n}\Delta t \tag{3}$$

Secondly, a rotation step is included using the magnetic field calculated at $\mathbf{x}^{n+1/2}$ location,

$$\mathbf{u^{n+1}} = \mathbf{u^n} + (\mathbf{u^n} + (\mathbf{u^n} \times \boldsymbol{\tau})) \times \mathbf{s} \tag{4}$$

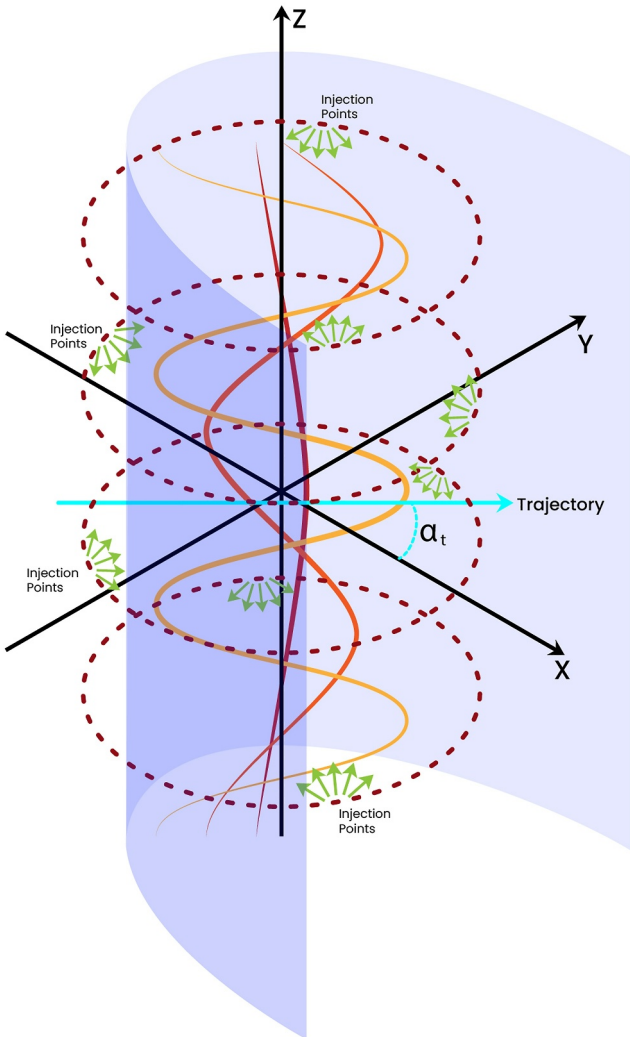

Figure 1. Sketch of the numerical simulations setup. The magnetic flux ropes lines are represented by the maroon, red and orange helical curves along the *Z*–direction; the blue surface corresponds the shock wave; the injection point circumferences are shown in dashed brown lines; and the cyan line is the trajectory of observation. The green arrows represent the direction of the injected particles.

where $\boldsymbol{\tau} = \mathbf{B}(\mathbf{x}^{n+1/2})\,\frac{q\Delta t}{2m\gamma}$, $\mathbf{s} = 2\boldsymbol{\tau}/(1 + \boldsymbol{\tau}\cdot\boldsymbol{\tau})$. Then, the particle position is finally updated,

$$\mathbf{x}^{n+1} = \mathbf{x}^{n+1/2} + \frac{\mathbf{u}^{n+1}}{2\gamma}\Delta t \tag{5}$$

Note that, in the absence of an electric field the speed remains unchanged and consequently γ is constant along the integration process.

We carried out simulations in a cubic space with 1 au per side and using three different magnetic field configurations (Figure 1 shows a sketch of our simulations setup). The detailed simulations steps are in Appendix A but basically these are:

- **BG** Only background field (BG) consisting in a constant magnetic field magnitude of ∼10 nT, making an angle of 45° in the XY–plane (represented with dashed lines in the bottom panels of Figure 2). We note that this magnitude is higher than the mean (∼5 nT) but lies in the upper part (90 percentile) of the distribution of the solar wind magnetic field magnitude observed at 1 au (Klein & Vech, 2019), and was chosen to emphasize the impact of this field over the charged particles.
- **MFR** In this case we added to the BG magnetic field a cylindrical magnetic flux rope field (MFR), represented by the maroon, red and orange helical curves in Figure 1 and the continuous lines in the bottom panels of Figure 2, with a radius of 0.16 au; a maximum magnitude of 20 nT; its axis aligned with the *Z*–axis; and centered at the coordinate system origin. The total magnetic field and its components showing the field rotation are plotted in panels (c and d) Figure 2. The MFR is imposed following the equations described by Lundquist (1951).
- **MFRSH** We impose a sheath region, as an enhancement in the BG field at one side of the MFR. This field has a cylindrical-parabolic topology with the symmetry axis aligned with the *X*–axis and its vertex at 0.15 au away from the MFR border (blue surface in Figure 1 and continuous lines inside the beige shaded area in panel (d) of Figure 2).
- We added white noise of 10% to all the magnetic fields except in the ICME sheath region where we added a noise up to 20% of the amplitude. We note that there is not a typical value for these fluctuations, although we choose conservative values in agreement with Borovsky (2012) who, studying 10 years of the solar wind data, found that $\delta B/B = 0.16$ for slow SW and $\delta B/B = 0.21$ for CME plasmas.

Once the magnetic configuration is defined in the simulation space, we deployed a ring of injection points, that is, we set up 48 injection points forming a circumference with a radii of 3.5 au, centered at the coordinate system origin, with an angular separation of 7.6° (brown dash line circumferences in Figure 1). Each injection point ejects protons with 16 different energies (going from 10 to 160 GeV) toward the center of the MFR within 10 azimuth angles (from −80° to 80°); and 11 elevation angles, limited to the −45° to 45° range. For the sake of simplicity, we do not consider angles larger than ±45° due to the fact that most particles remain outside of the MFR. Both angles are measured from the radial line which connects the injection point with the center of the MFR (green arrows in Figure 1). To get a better idea of the 3D behavior of the system, we move the ring along the *Z*–direction in steps of 0.02 au from $z = -0.25$ au to $z = 0.25$ au.

We follow the trajectory of each particle and flag the particles that were deflected by the magnetic field toward the MFR–axis, i. e., particles whose V_z component is large enough to maintain a quasi-parallel *Z*–direction during 50 s (25 s before and 25 s after), during this time a 10 GeV proton travels a distance of ∼0.1 au. We flag the total

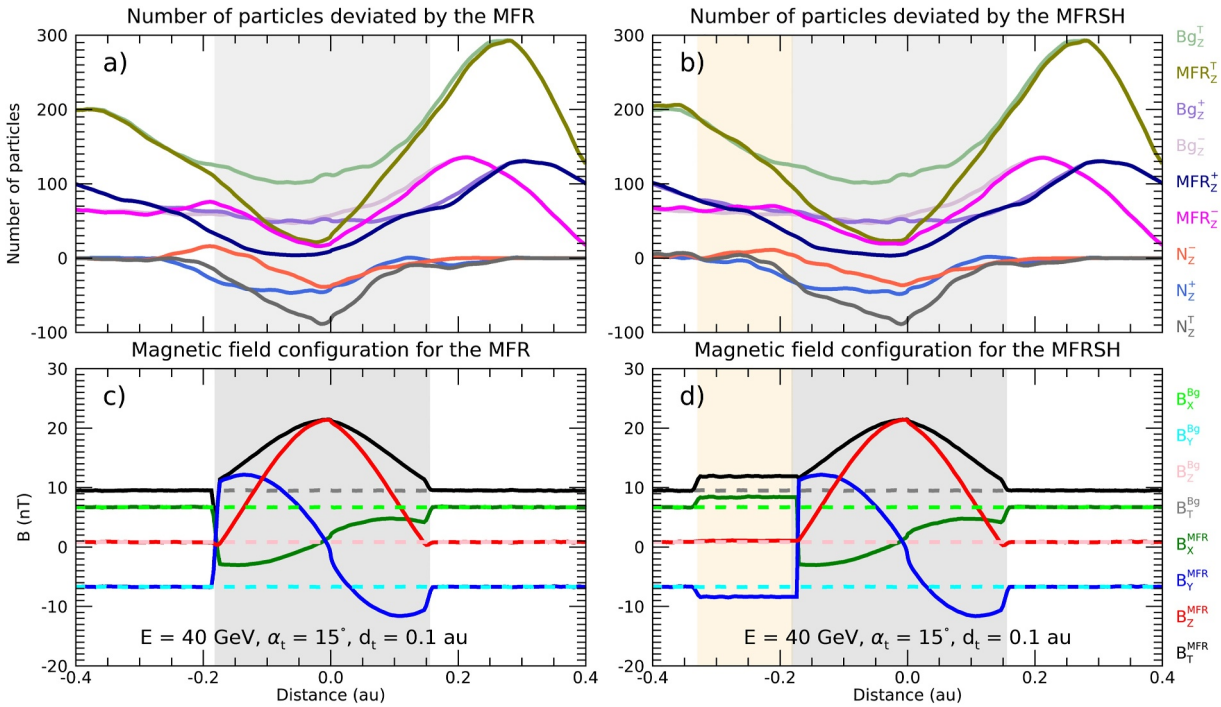

Figure 2. The upper panels show the number of particles deviated by the magnetic flux ropes (MFR), and traveling ∼0.1 au along the *Z*–axis toward positive (+), negative (−) and both (T) directions. The simulation of the BG case is represented by the purple (+), thistle (−) and sea-green (T) curves. Whereas, the olive (T), dark-blue (+) and magenta (−) curves, represent the simulations of the MFR and MFRSH (panel a, b, respectively). The result of the subtraction, that is, MFR–BG and MFRSH–BG (panel a, b, respectively) are shown by the gray (T), royal-blue (+) and tomato (−) curves. The bottom panels show the total magnetic field and its components for the BG (gray cyan, light-green, and pink dashed lines for B_T, B_x, B_y and B_z, respectively). And the black, dark-green, blue and red curves represent the magnetic field (B_T, B_x, B_y and B_z, respectively) assumed for the MFR (c) and MFRSH (d) panels. These examples correspond to simulations of particles with energy of 40 GeV and an impact distance and angle values of 0.1 au and 15°. The gray shaded areas mark the MFR and the beige shadow areas on the right panels mark the SH.

number of particles traveling in direction quasi-parallel to the *Z*–axis as well as the particles going in positive and negative *Z*–direction.

Then in each point of the XY–plane, we integrate the flagged particles (total, positive and negative) along the *Z*–direction (from $z = -0.25$ au to $z = 0.25$ au). Next, we define the trajectories of observations, these are, line cuts that mimic the trajectory of a detector crossing the MFR at distance d_t (measured from the MFR center), in a straight line that lies in the XY–plane and makes an angle α_t with respect to the positive *X*–axis (cyan line in Figure 1). Finally, we count the number of flagged particles along each trajectory.

3. Results

The number of particles deviated toward the *Z*–direction were counted along lines resembling the trajectories of the Earth or one spacecraft crossing the MFR. These trajectories cross the MFR in a plane perpendicular to the MFR–axis in two directions, $\alpha_t = \pm 15°$ with respect to the *X*–axis. Taking in to account that the BG field is at −45°, these directions make an angle of 60° and 30° with the BG magnetic field direction. In each direction, the trajectories cut the MFR at two impact distances from the MFR–axis: $d_t = 0.1$ and 0.01 au. The results presented in the rest of the paper correspond to these (4) trajectories.

As examples, the upper panels of Figure 2 show the number of particles with 40 GeV of energy, going in the *Z*–direction as function of the distance to the MFR center, observed over a trajectory with $\alpha_t = 15°$ and $d_t = 0.1$ au. In both panels the total, positive and negative number of particles going in the *Z*–direction for the BG case are marked by the sea-green, purple and thistle curves, respectively. The MFR is marked with a gray shadow rectangular area and it is important to note that the observed increase of the number of particles outside of the MFR, at both extremes (∼200 and 300 particles at distances of ∼ −0.36 and ∼0.26 au), these are artifacts created by the limitations on the simulations set up, and are due to the fact that the low energy particles injected in directions quasi-parallel to the BG magnetic field, are forced to follow these lines creating the observed excess in all

simulations runs, that is, only BG, BG + MFR and BG + SH + FR. This artifact is canceled when we subtract the BG to the MFR and SHFR runs. The dark-blue, magenta and olive curves represent the number of particles going toward positive, negative and both Z–directions for the cases of MFR and MFRSH, panels (a) and (b) panels of Figure 2, respectively.

There is a clear effect of the MFR over the charged particles observed close to the coordinate system origin ($\sim d = 0$ au) where the total number of MFR particles is significantly lower than the total number of BG particles. Furthermore, it is important to note that the difference between BG and MFR particles is larger for the particles going in the Z+ than *Z*–direction. In contrast the number of particles are similar for the MFR and BG cases at larger distances ($d > \pm 0.2$ au).

In order to obtain the best representation of the effect of the MFR magnetic field over the charged particles, we have subtracted the BG number of particles to the MFR and MFRSH numbers of particles. The gray, royal-blue and tomato curves in the upper panels of Figure 2, represent the number of particles traveling quasi-parallel to the *Z*–axis with positive $\left(N_Z^+ = FR_Z^+ - BG_Z^+\right)$; negative $\left(N_Z^- = FR_Z^- - BG_Z^-\right)$; and both $\left(N_Z^T = FR_Z^T - BG_Z^T\right)$ directions.

The gray curve $\left(N_Z^T\right)$ resembles the observed decrease of GCR during a Forbush decrease. Although, in this case we only are taking into account particles deviated toward the *Z*–direction (ignoring particles in the X– and *Y*–direction which are important in the Forbush decreases). The royal-blue $\left(N_Z^+\right)$ and tomato $\left(N_Z^-\right)$ curves represent the anisotropic flux of particles deviated by the MFR toward the $\pm$ *Z*–direction.

The lower panels of Figure 2 show the magnetic field implemented to simulate the BG (dashed curves) as well as the MFR and MFRSH (continuous curves in panels (c and d), respectively), the colors represent the total (black), and x, y, z components (blue, green and red curves, respectively), magnetic field. Panel (c) shows the case when only a MFR is present and the magnetic field rotation of the components of the field is clearly seen. The case of the MFR plus the sheath (MFRSH) is shown in panel (d), where a slight enhancement of the magnetic field is seen starting at -0.35 au and ending at -0.2 au, where the MFR starts. In all cases, the gray-shadow area delimits the MFR while the beige-shadow area corresponds to the ICME sheath.

Figure 2 shows in detail the simulations results for 40 GeV particles, whereas examples of the simulated number of particles for the rest of energies are presented in Figure 3 (Note that negative numbers of N_Z^T implies a deficit of particles with respect to the background), the curves of each analyzed energy are labeled with the color code shown in the right side of the figure. The thick cyan line corresponds to the total number of particles obtained by adding the number of particles computed at each considered energy (from 10 to 160 GeV) and scaled by the power law function $N(E) = N_0\left(\frac{E}{E_0}\right)^{-2.7}$ where N is the number of particles, E the energy and $N_0 = 501$ particles is obtained when assuming $N = 1$ and $E_0 = 10$ GeV.

Left and right panels of Figure 3 correspond to a trajectory crossing the MFR at an angle $\alpha_t = -15°$ and $d_t = 0.1$ *au*; and the MFRSH at angle $\alpha_t = 15°$ and an impact distance of $d_t = 0.01$ *au*. The beige and gray shadow areas mark the SH and MFR zones, respectively. As expected, the effect of the MFR on the CR number depends on its energy, low energy CR are suppressed close to the center of the MFR and we count a reduction up to $\sim$100 particles less than the background. It is interesting to note that there is an energy threshold at 120 GeV, where particles with energy higher than this threshold do not suffer large effect (diminishing) due to the MFR. This threshold must be function of the MFR strength and will be investigated in future works. Another interesting feature is the gradual decrease of the number of particles inside the sheath (orange shadowed area) as compared with the opposite side of the MFR where only the ambient magnetic field is present and there is no particle decrease outside the MFR.

The middle panels of Figure 3 show the relative difference of the number of particles traveling in the *Z*–direction and defined as, $D_r = \left(N_Z^+ - N_Z^-\right)/\left(N_Z^+ + N_Z^-\right)$, plotted as function of the distance to the center of MFR for each simulated energy. Even though that it is possible to see defined peaks of the D_r inside the MFR and SH, this becomes noise outside of the structures of interest due to the fact that the number of particles goes to zero at these regions.

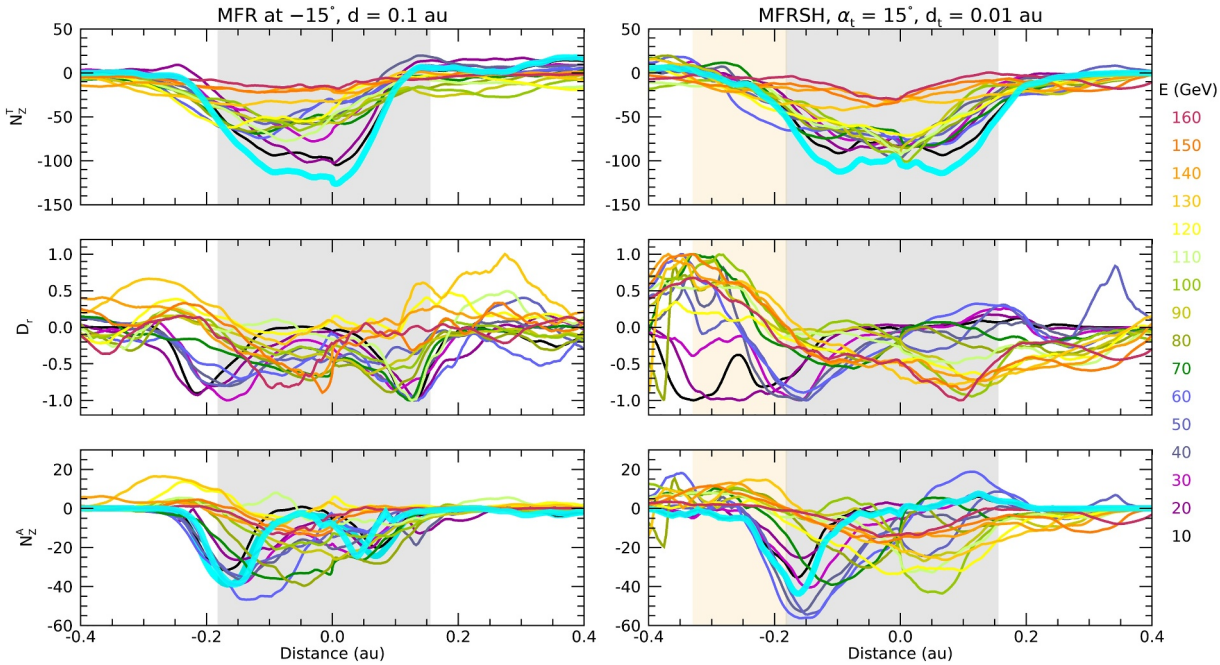

Figure 3. Top panels show the total number of particles $\left(N_Z^T\right)$ traveling parallel to the *Z*–direction for all energies as marked by the color code at the right of the figures. The computed relative differences (D_r) for each energy are plotted in the middle panels. The asymmetric number of particles $\left(N_Z^A = D_r|N_Z^T|\right)$ are shown in the bottom panels. The cyan thick curves represent the scaled sum of particles (see the Text in Supporting Infromation S1).

Observationally, the number of asymmetric particles defined as $N_Z^A = D_r|N_Z^T|$, is more relevant than the relative difference and therefore, this anisotropy is plotted in the bottom panels of Figure 3. The N_Z^A shows important features:

- There is a clear anisotropy inside the MFR and part of the ICME sheath.
- The anisotropy has regular behavior with a well defined increase, peak and decrease of N_Z^A.
- The anisotropy depends on the energy and the detector location inside the MFR.
- The sheath region makes an important change in the anisotropy as compared with the MFR–BG boundary.

The wide cyan curve in these figures represent the scaled sum of all energies and is similar to the asymmetry that an observer without energy discrimination will detect when crossing a MFR. In contrast, an observer with energy discrimination capability, will observe anisotropy peaks at different distances inside the MFR depending on the particle energy. More examples of the anisotropies "observed" in different trajectories inside the MFRSH and MFR can bee seen in (Lara, 2024).

A comprehensive view of the anisotropy generated by the MFR is presented in Figure 4 where the position (upper panels) and amplitude (bottom panels) of the peak of the anisotropic flux are plotted as function of the particle energy. The four trajectories crossing the MFR are represented by different colors for both cases; MFR and MFRSH on the left and right panels of Figure 4.

The deviation of charged particles due to the MFR depends on the energy of the particles as:

- **Low:** The anisotropy peak of particles with energy ≤70 GeV is confined to the inner limit of the MFR–sheath and MFR–BG interfaces, at d ∼ − 0.2 au. This anisotropy is due to the large discontinuity of the B_x and B_y components at this distance, as seen in the bottom panels of Figure 2. Note that the transition between these components is smoother on the opposite border of the MFR. The amplitude of the peak increases with the energy up to ∼60 GeV where the maximum amplitude is reached.
- **Medium:** The anisotropic peak of particles with energy in the 70–130 GeV range is situated close to the MFR–axis but at positive distances, where the BG–MFR transition is smoother. In this case the amplitude of the peaks decrease with the energy.

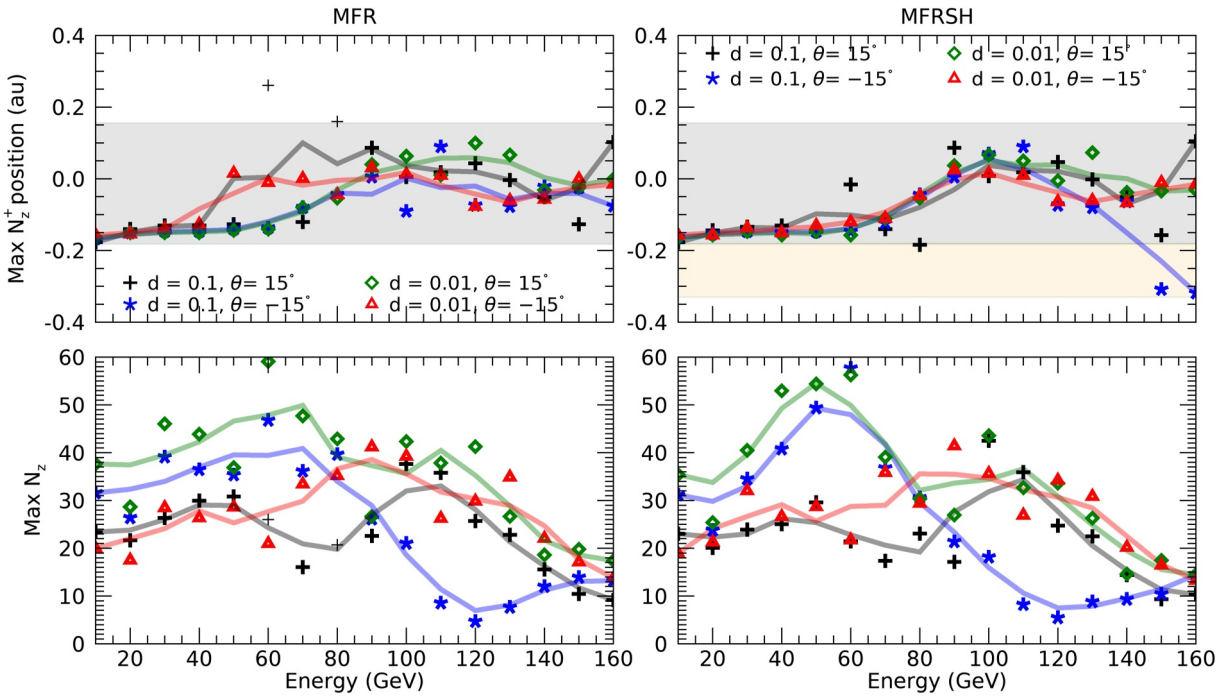

Figure 4. Characterization of the anisotropy peak in terms of the energy, the position (upper panels) and the amplitude (bottom panels) computed for the four trajectories: black plus and blue stars corresponding to impact distance of 0.1 au and angles of 15° and −15°, respectively; green diamonds and red triangles correspond to a closer impact distance of 0.01 au and same angles of 15° and −15°, respectively. The curves represent the smoothed version of the same points. The left and right panels correspond to the magnetic flux ropes and MFRSH cases, respectively.

- **High:** The amplitude of the anisotropic peak for particles with energy higher than 130 GeV is low (<20 particles) and the position is randomly distributed, which means that the effect of the MFR on the high energy particles is negligible.

As future work we have to analyze particular events taking into account all observed ICME parameters, but the fact that the number of anisotropic particles seen in the lower panels of Figure 3 resembles the anisotropy observed with world wide networks of neutron and muon detectors and air shower arrays makes us think that our model is correct and that it is worth investigating this phenomenon further.

As instance, Munakata et al. (2022) reported important anistropies observed by muon and neutron detectors during the passage of an ICME on November 2021. They found that the peak position and amplitude of the anistropies depend on the rigidity of the particles as seen in panels (a) and (e) of Figure 3 of that paper where the anistorpies measured at ∼15 and ∼60 GV (corresponding to proton energies of ∼13.97 and ∼58.59 GeV) are shown, respectively. Furthermore the anisotropy direction is well related with the direction of the interplanetary magnetic field as seen in panels (b) and (c) of the same figure.

Another example is the large GCR enhancement detected by HAWC during the passage of an ICME on October 2016, shown in Figure 3 of Akiyama et al. (2020). The authors claim that the high sensitivity of this array allowed the detection of the enhancement produced by a GCR anisotropy caused by the MFR helical field. The enhancement showed a double peak coincident with the arrival time of the MFR trailing part. The double peak was caused by anisotropies of particles with different energy.

Note that in this work, we are not attempting to reproduce these events but there are similarities between Munakata et al. and Akiyama et al. events with our results for low energy (10–80 GeV) anisotropies as shown at the bottom panels of Figure 3, and similar Figures for other crossing paths that can be found in the electronic supporting material (Lara, 2024).

4. Conclusions

We investigate the ability of large scale (few tenths of an astronomical unit) magnetic structures with a well defined helical magnetic topology known as MFR, to deviate the otherwise isotropic flux of galactic charged particles and produce an anisotropic flux of these particles.

In this work, we simulated a constant background magnetic field; a cylindrical-helical MFR and a cylindrical-parabolic sheath region with enhanced constant magnetic field. Then protons of energy in the 10–160 GeV range were injected all around the cylindrical structure and their trajectory was followed, if any particle traveled more than 0.1 au along the axis of the MFR in positive or negative direction was flagged and the anisotropic flux was defined in terms of these particles. Finally, the number of anisotropic particles was computed along a set of observation trajectories (straight lines crossing the MFR perpendicularly to its axis, at different distances and angles).

We find that: There is an evident anisotropy in the flow of charged particles imposed by the MFR which guides the particles toward a direction quasi-parallel to its axis. The amplitude and position of the anisotropy peak depends on the energy of the particle; the angle between the BG and MFR fields; and the presence of a sheath region.

The guided flux of GCR explains naturally the presence of the precursors or GCR enhancements often seen prior the arrival at 1 au of ICMEs. Furthermore, this anistropic flux explains the GCR enhancement observed by neutron monitors since the 50s of the last century and that until now remains without a clear explanation, as well as the GCR enhancement recently observed by HAWC during the passage of an interplanetary magnetic flux rope.

Appendix A: Methodology

The steps followed to obtain the asymmetry of protons due to the MFR are as follows:

1. Define the ambient magnetic field, in this case $B_{BG} = (0.7, -0.7, 0.1)$, this is a magnetic field of ∼10 nT, with an angle of −45° in the XY–plane.
2. Define the MFR structure, centered at the origin and with its axis parallel to the Z–axis, with a maximum magnetic field of 21 nT along its axis.
3. Add white noise of 10% of the magnetic field amplitude.
4. In the case of SHFR, define a parabolic region at the front of the MFR at a distance (at the apex) of 1.4 au. from the MFR border.
5. Generate injection points where protons with energy between 10 and 160 GeV are expelled at 10 azimuth angles varying from −80° to 80°; and at 11 elevation angles ranging from −45° to 45° with steps of 15°. Both angles are measured from the line going from injection point to the center of the MFR.
6. Distribute a set of injection points in a ring around the MFR at a distance of 0.5 au with an angular distance of 7.5° between the injection points.
7. Generate the injection volume (cylinder) by moving the injection rings along the Z–direction, from −0.25 to 0.25 au in 25 steps of 0.02 au.
8. Follow the trajectory of each particle and label the particles which remain in the $\pm Z$ direction during 50 s, i.e., a distance of at least ∼0.1 au (this is approximately the distance traveled by a 10 GeV in 50 s).
9. Define the "observation" trajectories as straight lines crossing the MFR, embedded in the plane perpendicular to the MFR–axis, at two angles ±15° measured from the positive X–axis and at two impact distances: 0.01 and 0.1 au, measured (perpendicularly) between the trajectory and the MFR–axis.
10. Setting up 500 "observation" points along each trajectory and count the labeled particles (in step 8) which crosses a circular area of 0.009 au radius around each point. The counted particles are reported as N_Z^i, where $i = -, +, T, A$, throughout the work.

Data Availability Statement

The simulations code is available at github (Guennam, 2024). The data and the software to analyze and visualize the results presented in this work is available in (Lara, 2024).

Acknowledgments
A. Lara thanks UNAM-PAPIIT-IN110524 Grant for partial support. TN was partially supported by NASA 80NSSC22K0225 Grant. We thank Angélica Espinosa and Minerva Castro Escamilla for their technical support. We would like to thank the anonymous referees for their help improve the manuscript.

References

Abeysekara, A. U., Albert, A., Alfaro, R., Alvarez, C., Álvarez, J. D., Araya, M., & HAWC Collaboration. (2023). The High-Altitude Water Cherenkov (HAWC) observatory in México: The primary detector. *Nuclear Instruments and Methods in Physics Research*, *1052*, 168253. https://doi.org/10.1016/j.nima.2023.168253

Akiyama, S., Alfaro, R., Alvarez, C., Angeles Camacho, J. R., Arteaga-Velázquez, J. C., Arunbabu, K. P., et al. (2020). Interplanetary magnetic flux rope observed at ground level by HAWC. *ApJ*, *905*(1), 73. https://doi.org/10.3847/1538-4357/abc344

Alania, M. V., Modzelewska, R., & Wawrzynczak, A. (2011). On the relationship of the 27-day variations of the solar wind velocity and galactic cosmic ray intensity in minimum epoch of solar activity. *Solar Physics*, *270*(2), 629–641. https://doi.org/10.1007/s11207-011-9778-6

Altukhov, A. M., Kuzmin, A. I., Krimsky, G. F., Skripin, G. V., & Chirkov, N. P. (1963). On the rotation of cosmic ray anisotropy. *International cosmic ray conference*, *3*, 421.

Alvarez, C., Angeles Camacho, J. R., Arteaga-Velázquez, J. C., Arunbabu, K. P., Avila Rojas, D., Baghmanyan, V., et al. (2021). HAWC as a ground-based space-weather observatory. *Solar Physics*, *296*(6), 89. https://doi.org/10.1007/s11207-021-01827-z

Arunbabu, K. P., Antia, H. M., Dugad, S. R., Gupta, S. K., Hayashi, Y., Kawakami, S., et al. (2013). High-rigidity forbush decreases: Due to CMEs or shocks? *A&A*, *555*, A139. https://doi.org/10.1051/0004-6361/201220830

Arunbabu, K. P., Antia, H. M., Dugad, S. R., Gupta, S. K., Hayashi, Y., Kawakami, S., et al. (2015). How are Forbush decreases related to interplanetary magnetic field enhancements? *A&A*, *580*, A41. https://doi.org/10.1051/0004-6361/201425115

Aslam, O. P. M., & Badruddin (2012). Solar modulation of cosmic rays during the declining and minimum phases of solar cycle 23: Comparison with past three solar cycles. *Solar Physics*, *279*(1), 269–288. https://doi.org/10.1007/s11207-012-9970-3

Aslam, O. P. M., & Badruddin (2015). Study of cosmic-ray modulation during the recent unusual minimum and mini-maximum of solar cycle 24. *Solar Physics*, *290*(8), 2333–2353. https://doi.org/10.1007/s11207-015-0753-5

Bhaskar, A., Vichare, G., Arunbabu, K. P., & Raghav, A. (2016). Role of solar wind speed and interplanetary magnetic field during two-step Forbush decreases caused by Interplanetary Coronal Mass Ejections. *Ap&SS*, *361*(7), 242. https://doi.org/10.1007/s10509-016-2827-8

Boris, J. P. (1970). Relativistic plasma simulation-optimization of a hybrid code. In *Fourth conference numerical simulations of plasmas* (Vol. 3).

Borovsky, J. E. (2012). The velocity and magnetic field fluctuations of the solar wind at 1 au: Statistical analysis of fourier spectra and correlations with plasma properties. *Journal of Geophysical Research*, *117*(A5). https://doi.org/10.1029/2011JA017499

Burlaga, L., Sittler, E., Mariani, F., & Schwenn, R. (1981). Magnetic loop behind an interplanetary shock: Voyager, Helios, and IMP 8 observations. *JGR*, *86*(A8), 6673–6684. https://doi.org/10.1029/JA086iA08p06673

Cane, H. V. (2000). Coronal mass ejections and Forbush decreases. *Space Science Reviews*, *93*, 55–77. https://doi.org/10.1023/A:1026532125747

Davies, E. E., Scolini, C., Winslow, R. M., Jordan, A. P., & Möstl, C. (2023). The effect of magnetic field line topology on ICME-related GCR modulation. *ApJ*, *959*(2), 133. https://doi.org/10.3847/1538-4357/ad046a

Dialynas, K., Sterken, V. J., Brandt, P. C., Burlaga, L., Berdichevsky, D. B., Decker, R. B., et al. (2023). A future Interstellar Probe on the dynamic heliosphere and its interaction with the very local interstellar medium: In-situ particle and fields measurements and remotely sensed ENAs. *Frontiers in Astronomy and Space Sciences*, *10*, 58. https://doi.org/10.3389/fspas.2023.1061969

Dorman, L. (2006). Cosmic ray interactions, propagation, and acceleration in space plasmas (Vol. *339*). https://doi.org/10.1007/978-1-4020-5101-2

Dumbović, M., Vršnak, B., Čalogović, J., & Župan, R. (2012). Cosmic ray modulation by different types of solar wind disturbances. *A&A*, *538*, A28. https://doi.org/10.1051/0004-6361/201117710

Forbush, S. E. (1937). On the effects in cosmic-ray intensity observed during the recent magnetic storm. *Physical Review*, *51*, 1108.

Gaisser, T. K., Engel, R., & Resconi, E. (2016). *Cosmic rays and particle physics* (2nd ed.). Cambridge University Press.

Guennam, E. (2024). Flux rope and cosmic rays interaction simulations code [simulations code]. *github*. Retrieved from https://github.com/aegtuc/MagneticPPusher

Guo, X.-C., Jiang, W., & Li, H. (2021). Statistical investigation on galactic cosmic rays and solar wind variation based on ACE observations. *ChA&A*, *45*(2), 147–161. https://doi.org/10.1016/j.chinastron.2021.05.002

Kilpua, E. K. J., Lugaz, N., Mays, M. L., & Temmer, M. (2019). Forecasting the structure and orientation of earthbound coronal mass ejections. *Space Weather*, *17*(4), 498–526. https://doi.org/10.1029/2018SW001944

Klein, K. G., & Vech, D. (2019). Solar Wind Plasma Parameter Distributions at 1 au. *Research Notes of the American Astronomical Society*, *3*(7), 107. https://doi.org/10.3847/2515-5172/ab3465

Kubo, Y., & Shimazu, H. (2010). Effect of finite larmor radius on the cosmic ray penetration into an interplanetary magnetic flux rope. *The Astrophysical Journal*, *720*, 853–861.

Laitinen, T., & Dalla, S. (2021). Access of energetic particles to a magnetic flux rope from external magnetic field lines. *The Astrophysical Journal*, *906*(9), 10.

Lara, A. (2024). Flux rope and cosmic rays interaction data and analysis tools [Dataset]. *UNAM, Instituto de Geofísica*. Retrieved from http://132.248.182.110/resources/LARA_A/

Lara, A., Gopalswamy, N., Caballero-López, R. A., Yashiro, S., Xie, H., & Valdés-Galicia, J. F. (2005). Coronal mass ejections and galactic cosmic-ray modulation. *ApJ*, *625*(1), 441–450. https://doi.org/10.1086/428565

Luhmann, J. G., Gopalswamy, N., Jian, L. K., & Lugaz, N. (2020). ICME evolution in the inner heliosphere. *Solar Physics*, *295*(4), 61. https://doi.org/10.1007/s11207-020-01624-0

Lundquist, S. (1951). On the stability of magneto-hydrostatic fields. *Physical Review*, *83*(2), 307.

Marubashi, K. (2000). Physics of interplanetary magnetic flux ropes: Toward prediction of geomagnetic storms. *Advances in Space Research*, *26*(1), 55–66. https://doi.org/10.1016/S0273-1177(99)01026-1

Munakata, K., Bieber, J. W., Yasue, S.-i., Kato, C., Koyama, M., Akahane, S., et al. (2000). Precursors of geomagnetic storms observed by the muon detector network. *JGR*, *105*(A12), 27457–27468. https://doi.org/10.1029/2000JA000064

Munakata, K., Kozai, M., Kato, C., Hayashi, Y., Kataoka, R., Kadokura, A., et al. (2022). Large-amplitude bidirectional anisotropy of cosmic-ray intensity observed with worldwide networks of ground-based neutron monitors and muon detectors in 2021 November. *ApJ*, *938*(1), 30. https://doi.org/10.3847/1538-4357/ac91c5

Nieves-Chinchilla, T., Jian, L. K., Balmaceda, L., Vourlidas, A., dos Santos, L. F. G., & Szabo, A. (2019). Unraveling the internal magnetic field structure of the Earth-directed interplanetary coronal mass ejections during 1995–2015. *Solar Physics*, *294*(7), 89. https://doi.org/10.1007/s11207-019-1477-8

Petukhova, A. S., Petukhov, I. S., & Petukhov, S. I. (2019). Theory of the formation of forbush decrease in a magnetic cloud: Dependence of forbush decrease characteristics on magnetic cloud parameters. *The Astrophysical Journal*, *880*(17), 12.

Ripperda, B., Bacchini, F., Teunissen, J., Xia, C., Porth, O., Sironi, L., et al. (2018). A comprehensive comparison of relativistic particle integrators. *The Astrophysical Journal - Supplement Series*, *235*(1), 21. https://doi.org/10.3847/1538-4365/aab114

Rockenbach, M., Dal Lago, A., Gonzalez, W. D., Munakata, K., Kato, C., Kuwabara, T., et al. (2011). Geomagnetic storm's precursors observed from 2001 to 2007 with the global muon detector network (GMDN). *GRL*, *38*(16), L16108. https://doi.org/10.1029/2011GL048556

Subramanian, P., Antia, H. M., Dugad, S. R., Goswami, U. D., Gupta, S. K., Hayashi, Y., et al. (2008). Forbush decreases and turbulence levels at coronal mass ejection fronts. *Astronomy&Astrophysics*, *494*(3), 1107–1118.

Thomas, S. R., Owens, M. J., & Lockwood, M. (2014). The 22-year Hale cycle in cosmic ray flux - Evidence for direct heliospheric modulation. *Solar Physics*, *289*(1), 407–421. https://doi.org/10.1007/s11207-013-0341-5

Usoskin, I. G., Braun, I., Gladysheva, O. G., Hörandel, J. R., Jämsén, T., Kovaltsov, G. A., & Starodubtsev, S. A. (2008). Forbush decreases of cosmic rays: Energy dependence of the recovery phase. *Journal of Geophysical Research*, *113*, A07102.

Van Allen, J. A. (2000). On the modulation of galactic cosmic ray intensity during solar activity cycles 19, 20, 21, 22 and early 23. *GRL*, *27*(16), 2453–2456. https://doi.org/10.1029/2000GL003792

Yoshida, S. (1959). Storm-time increase of cosmic-ray intensity. *Nature*, *183*(4658), 381–383. https://doi.org/10.1038/183381b0